Supporting Information

Polyoxometalate-Based Electron Transfer Modulation for Efficient Electrocatalytic Carbon Dioxide Reduction

Jing Du,[‡a] Zhong-Ling Lang, [‡a] Yuan-Yuan Ma,[‡a] Hua-Qiao Tan,[*a] Bai-Ling Liu,[a] Yong-Hui Wang,[a] Zhen-Hui Kang,[*b] and Yang-Guang Li [*a]

Table of Contents

1. Experimental Procedures

1.1 General Experimental Information

Reagents. $H_3PMo_{12}O_{40}\cdot nH_2O$, $H_3PW_{12}O_{40}\cdot nH_2O$, $H_4SiW_{12}O_{40}\cdot nH_2O$, Mn(bipy)$(CO)_3$Br and Ketchen Black (KB) were purchased from Aladdin Industrial Co., Ltd. Mn(bipy)$(CO)_3$Br and Nafion solution (5 wt%) were purchased from Alfa Aesar China (Tianjin) Co., Ltd. All chemicals were used as received without further purification. All solution used in experiments were prepared with Millipore water (18.2 MΩ). Cesium salt of $H_3PMo_{12}O_{40}\cdot nH_2O$, $H_3PW_{12}O_{40}\cdot nH_2O$, $H_4SiW_{12}O_{40}\cdot nH_2O$ were prepared by using simple co-precipitation method, denoted as Cs-PMo_{12}, Cs-PW_{12} and Cs-SiW_{12}.

Instrumentations. Infrared (IR) spectra were obtained on a Nicolet Magna 560 spectrometer with KBr pellets in the range of 4000–400 cm^{-1}. C, H and N elemental analyses were performed by Perkin-Elmer 2400 elemental analyzer; P, Si, Mo, W, Mn were acquired using a Prodigy XP emission spectrometer. Thermogravimetric (TG) analyses were performed on a TA SDT Q600 TG instrument at a heating rate of 10 °C min^{-1} from 25 to 800 °C in air atmosphere. X-ray powder diffraction (XPRD) data were collected on a Rigaku Smart Lab X-Ray diffractometer using Cu K_α radiation (λ = 1.5418 Å) in the 2θ range of 5–60° with a scanning rate of 2° per minute. Single crystal X-ray diffraction data was collected on a Bruker D8 Venture PHOTON 100 CMOS diffractometer equipped with graphite monochromated Mo K_α radiation (λ = 0.71073 Å). Nuclear magnetic resonance (NMR) spectra were recorded at room temperature on a Bruker INOVA-500 MHz NMR spectrometer. An inner tube containing D_2O was used as an instrumental lock. The transmission electron microscopy (TEM) was carried out a JEOL-2100 plus transmission electron microscope. The field-emission scanning electron microscopy (SEM) and the interrelated energy dispersive X-ray detector (EDX) spectra were carried out a Hitachi SU-8010 ESEM FEG scanning electron microscope. All electrochemical measurements were carried out on a CHI 760E electrochemical workstation at room temperature. The Fluorescence properties were measured on FLSP920 Edinburgh fluorescence spectrometer. The X-ray photoelectron spectroscopy (XPS) measurements were performed on a KRATOS Axis ultra DLD X-ray photoelectron spectrometer with a monochromatized Mg Kα X-ray source (hυ = 1283.3 eV). The elemental analyses for C, H and N were performed on a PerkinElmer 2400 CHN elemental analyzer. The nitrogen sorption measurement was obtained on an ASAP 2020 (Micromeritics, USA). The Brunauer-Emmett-Teller (BET) method was utilized to calculate the specific surface area by using adsorption data. The GC analyses were performed on Shimadzu GC-2014C gas chromatograph.

Single-crystal structure determination. The single-crystal structures of POM-MnL were solved by direct methods and refined by the full-matrix least-squares fitting on F^2 using Olex2 package,[1] the structure was solved with the ShelXS structure solution program using Direct Methods[2] and refined with the ShelXL-2018 refinement package using Least Squares minimization[3]. Crystal data and structure refinement parameters of **PW_{12}-MnL**, **PMo_{12}-MnL** and **SiW_{12}-MnL** are listed in Supplementary Table S1. In the final refinement, **SiW_{12}-MnL** exhibit with solvent accessible voids but no solvent molecules can be clearly assigned from the residual peaks. Thus, the SQUEEZE program was further used to remove the contributions of weak reflections to the whole data.[4] The new generated hkl data were further used to refine the final crystal data of **SiW_{12}-MnL**. Based on the elemental analysis, TG analysis, and the SQUEEZE calculation results, five CH_3CN molecules were directly included in the final molecular formula of SiW_{12}-MnL. Selected bond lengths and angles are listed in Supplementary Tables S2-4. Hydrogen bonds are listed in Supplementary Tables 5-7. The CCDC reference numbers are 1893118-1893120

Electrocatalytic activity test. Electrocatalytic activity tests were performed using a conventional three-electrode system. A platinum foil was used as a counter electrode and an Ag/AgCl (3.5 M KCl) was used as a reference electrode and converted to the RHE reference scale using E (vs. RHE) = E (vs. Ag/AgCl) + 0.2046 V + 0.059 V×pH. The working electrode was a catalyst-modified glassy carbon disk electrode (GCE, 3.0 mm diameter). The bulk electrolysis was performed in an airtight electrochemical H-type cell with three electrodes. H-type cell consists of two compartments separated by a Nafion® 117 anion exchange membrane with 50 mL 0.5 M $KHCO_3$ electrolyte in each chamber. Before electrolysis, the electrolyte in the cathodic compartment was degassed by bubbling with CO_2 gas (99.999 %) for at least 30 min (CO_2-saturated high purity aqueous 0.5 M $KHCO_3$). The electrolyte in the cathodic compartment was stirred at a rate of 600 rpm during electrolysis. CO_2 gas was delivered into the cathodic compartment at a rate of 20.00 sccm and was vented directly into the gas-sampling loop of a gas chromatograph (Shimadzu GC-2014C). The GC was equipped with two packed Porapak-N column and a packed Molecular sivev-13X column. Nitrogen (99.999%) was used as the carrier gas. The column effluent (separated gas mixtures) first passes through a thermal conductivity detector (TCD) where H_2 was quantified; Then, it passes through a methanizer where CO, CH_4, C_2H_4, C_2H_6 was converted to methane and subsequently quantified by a flame ionization detector (FID). The concentration of gaseous products was quantified by the integral area ratio of the reduction products to standards. The Faraday efficiency calculations refer to the published literature.[5] The CO partial current density at different potentials was calculated by multiplying the overall geometric current density and its corresponding faradic efficiency.

1.2 Computational Methods

All calculations were performed using the Gaussian program package with D1 version.[6] The computational scheme consists of two steps. In the first step, geometry optimizations for all intermediates and transition states were carried out at the B3LYP level without symmetry restrictions.[7,8] The LANL2DZ basis set was employed for the Mn, W, and Mo, whereas the 6-31G** basis set were used for the rest non-metal atoms (H, O, C, N, P, Si).[9-12] To confirm the stability of all structures, frequency calculations were performed at the same level as optimization. We can also obtain the thermal correction to the Gibbs free energy (ΔG_{corr}). In order to include the basis set and dispersion effects, single point calculations were conducted using a larger basis (6-311+G(2df,p) for H, O, C, N, P, Si) set and combining with the B3LYP-D3(BJ) approach, [13] which furnished more accurate electronic energies (E_{elec}). The sum of E_{elec} and ΔG_{corr} gives the final thermal free energy in solution. In all steps, the solvation effects were introduced to mimic an aqueous solution by using the PCM model.[14]

2. Supplementary Figures

Scheme S1 Ilustration of the preparation of **SiW_{12}-MnL** catalyst.

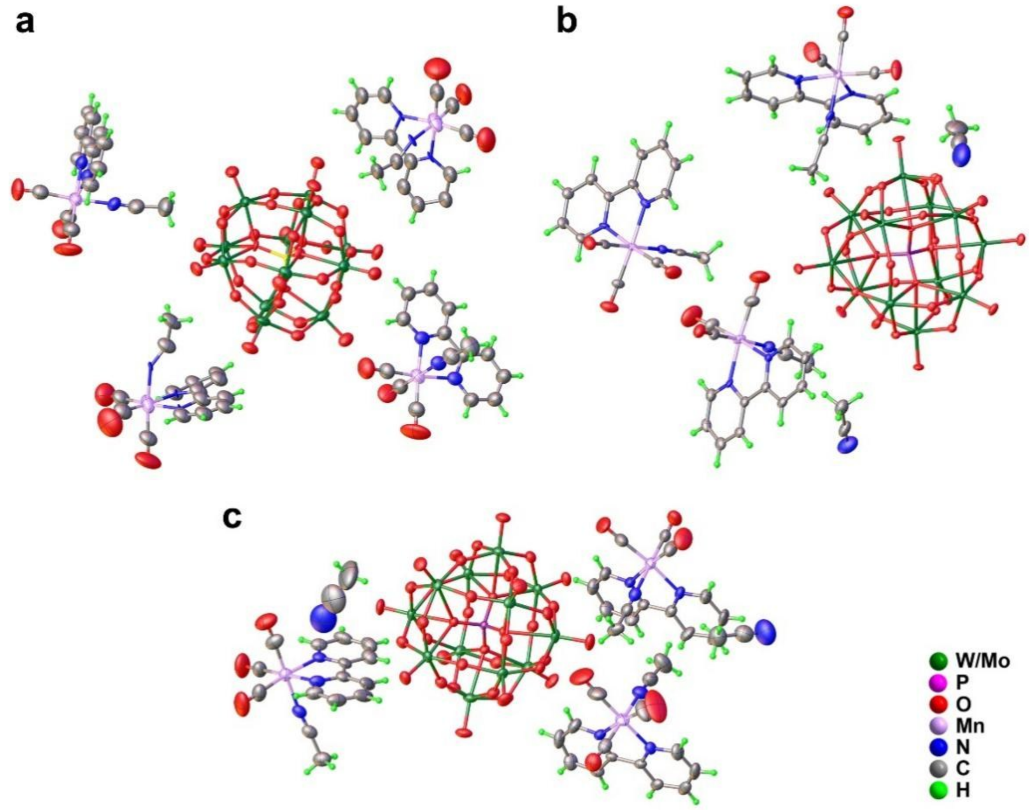

Figure S1 ORTEP view of the asymmetric unit of **SiW_{12}-MnL** (a), **PW_{12}-MnL** (b) and **PMo_{12}-MnL** (c) with thermal ellipsoids at 30 % probability displacement.

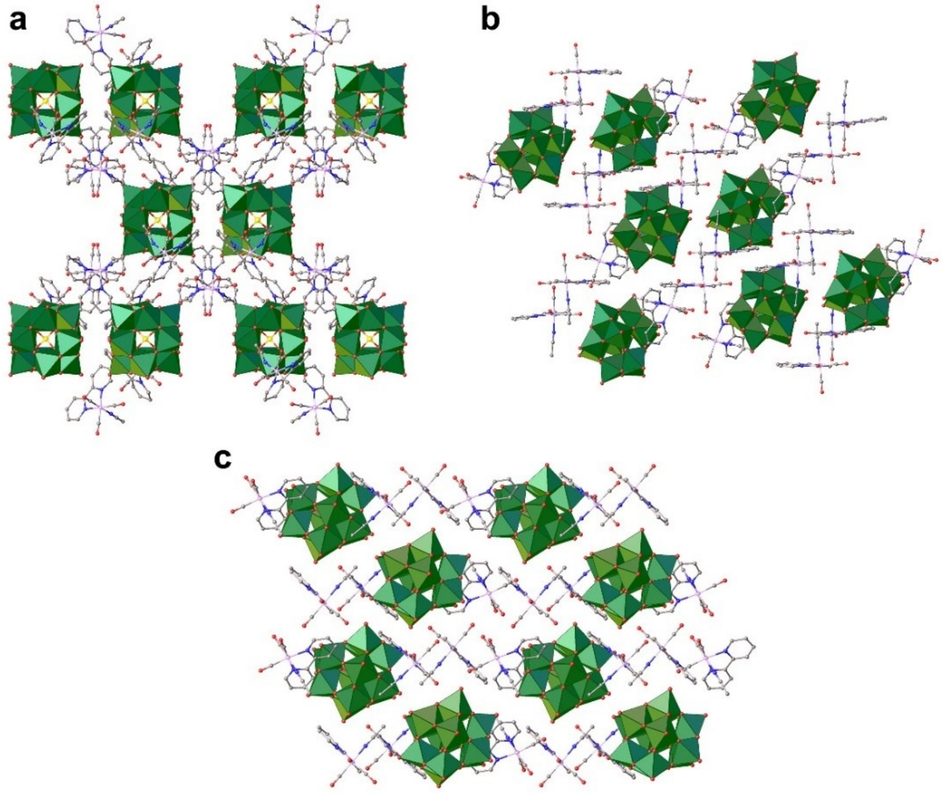

Figure S2 The packing arrangement of **SiW_{12}-MnL** (a), **PW_{12}-MnL** (b) and **PMo_{12}-MnL** (c) viewed along *a* axis (All H atoms are omitted for clarity).

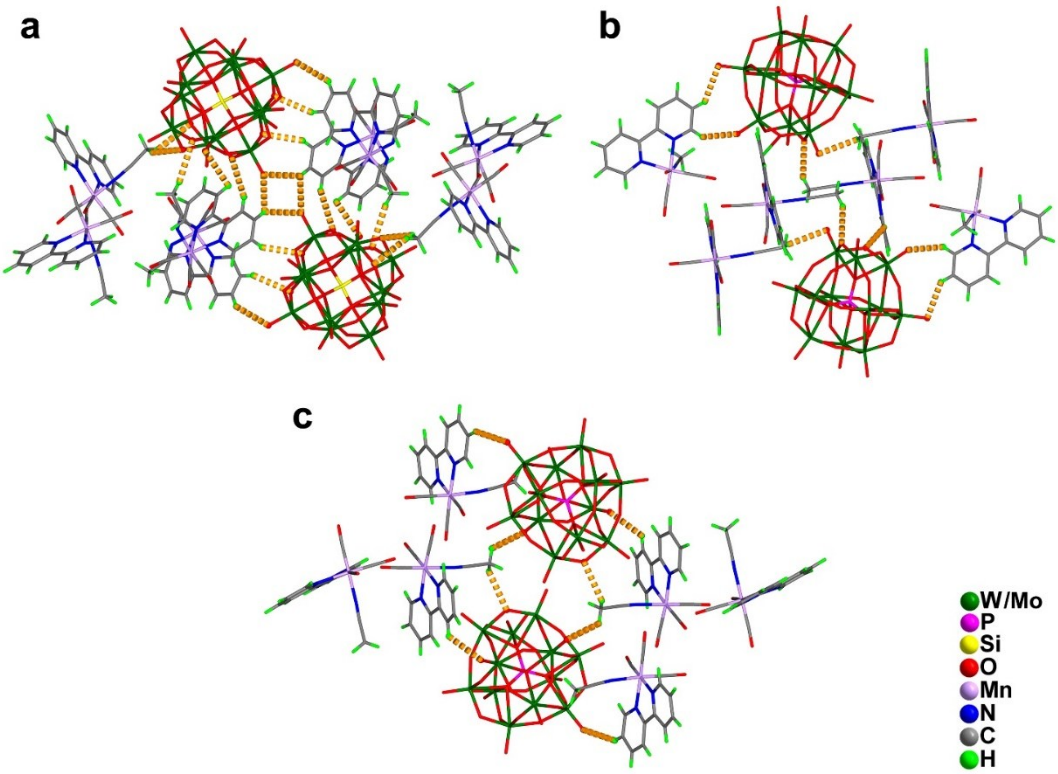

Figure S3 Hydrogen bonding (orange dotted lines) in the packing arrangement of **SiW_{12}-MnL** (a) **PW_{12}-MnL** (b) and **PMo_{12}-MnL** (c).

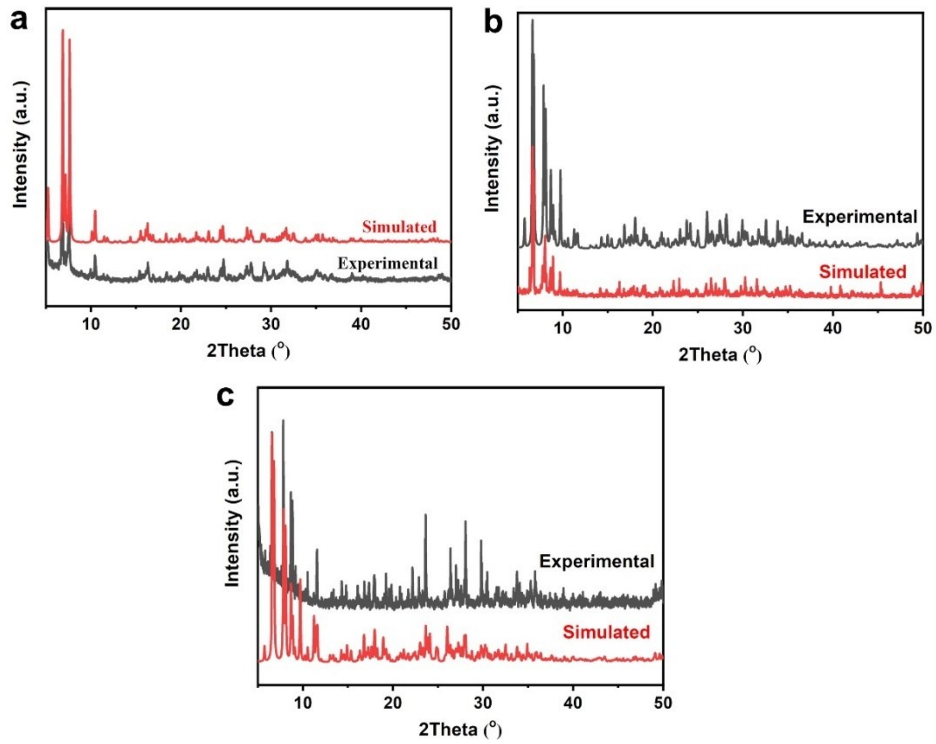

Figure S4 The powder X-ray diffraction patterns of **SiW_{12}-MnL** (a), **PW_{12}-MnL** (b) and **PMo_{12}-MnL** (c). Powder X–ray diffraction (PXRD, Figure S4) certified the structural integrity and phase purity of the crystalline POM-MnL composite catalysts, the experimental data are consistent with the simulated data are corresponded, which indicates that POM-MnL has been successfully prepared.

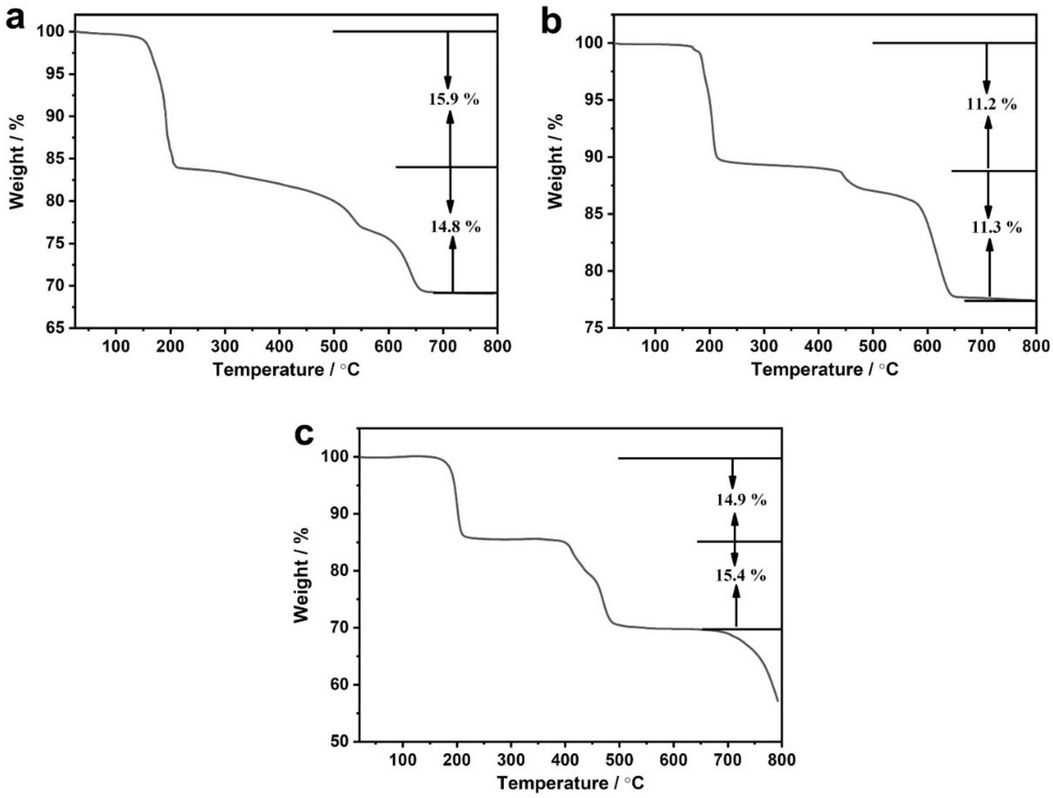

Figure S5 TG curves of **SiW_{12}-MnL** (a), **PW_{12}-MnL** (b) and **PMo_{12}-MnL** (c).

To further confirm the crystal structures and thermal stabilities, the TG curves of **POM-MnL** were also researched. As shown in Figure S5, all the **POM-MnL** can be stable at least 150 ^{o}C, taking **SiW_{12}-MnL** for example, there are two-step weight losses in the temperature range from 25 to 650 °C, the first weight loss from 25 to 215 °C is 15.9 % (Calcd. 15.72 %), which can be ascribed to the loss of all carbonyl and acetonitrile molecules. The second weight loss from 200 to 650 °C is 14.8 % (Calcd. 14.72 %), which is attributed to the loss of all 2, 2'-bipyridine molecules. These results indicated that the **POM-MnL** are stable at least below 150 °C.

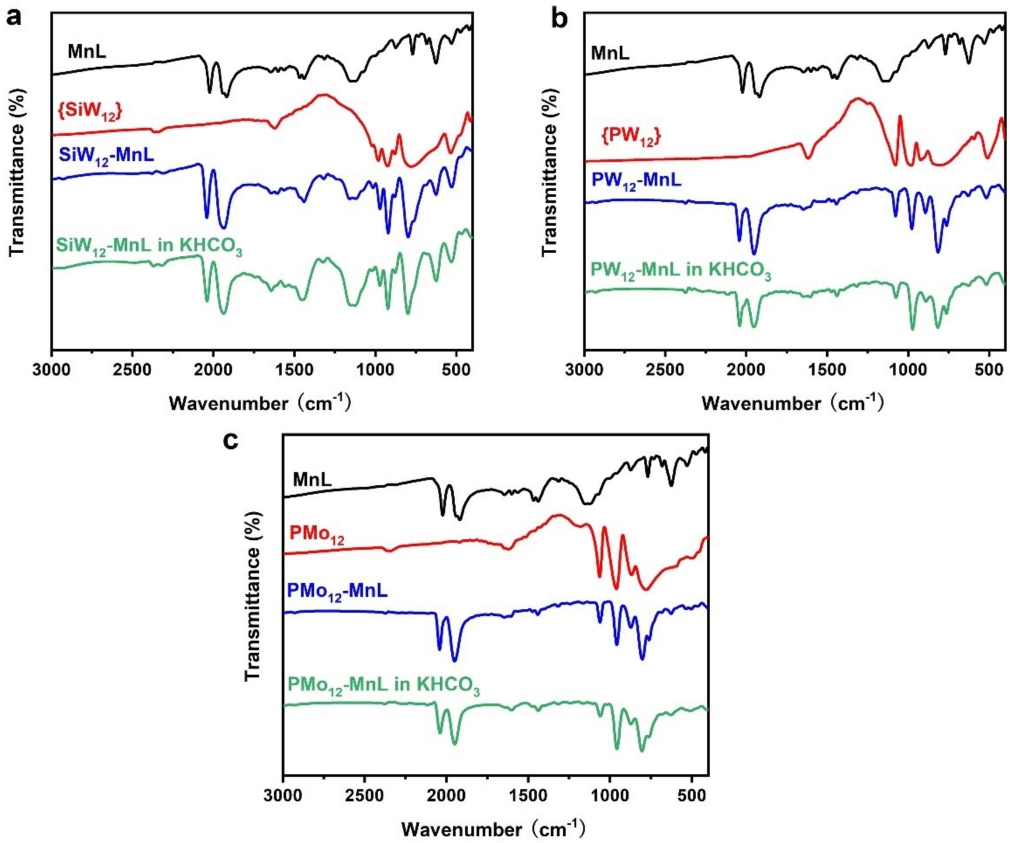

Figure S6. IR spectra of the POMs-MnL after soaking in 0.5 M $KHCO_3$ solution.

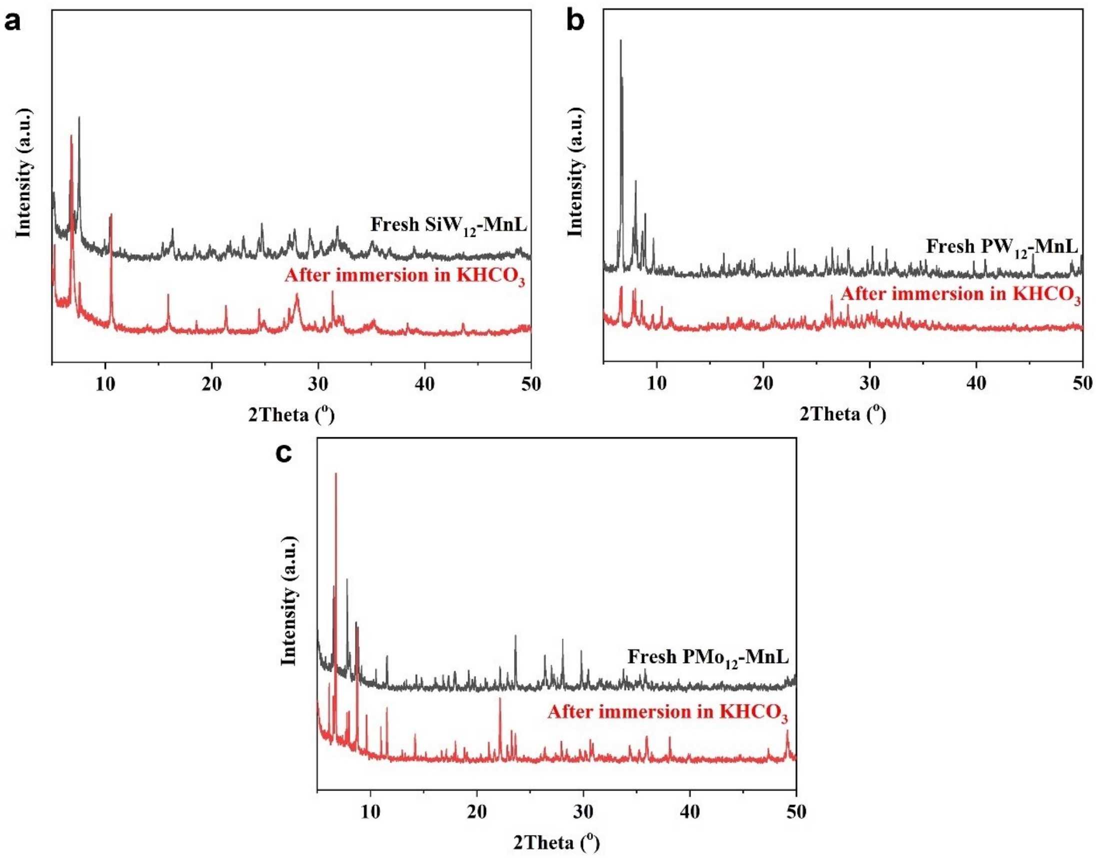

Figure S7. XRD patterns of the POMs-MnL after soaking in 0.5 M $KHCO_3$ solution.

As shown in Figure S6 and S7, the IR spectrum and XRD patterns of POM-MnL demonstrate that after soaking in CO_2-satuated $KHCO_3$ solution for 24 hours, the structure and composition of these POM-MnL composites do not show any change, the different intensities of peaks may be caused by the diverse preferred orientations of the powder samples, indicating the good stability of POM-MnL in CO_2-satuated $KHCO_3$ solution.

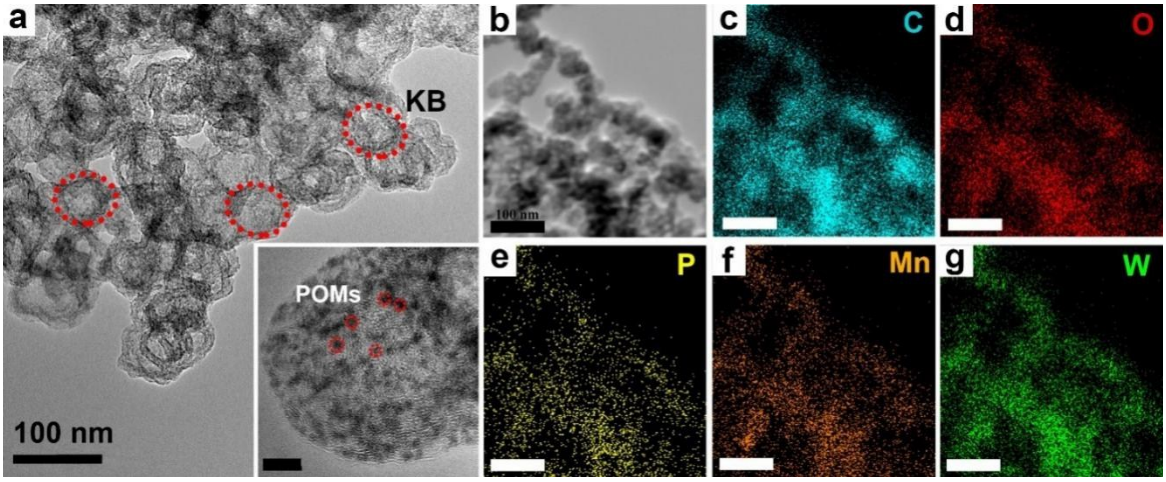

Figure S8 (a) TEM images of **PW_{12}-MnL** loaded on KB (inset: HR-TEM images of **PW_{12}-MnL/KB**, scale bar: 5 nm). (b–g) Corresponding elemental mapping of C, O, P, Mn and W of **PW_{12}-MnL/KB**.

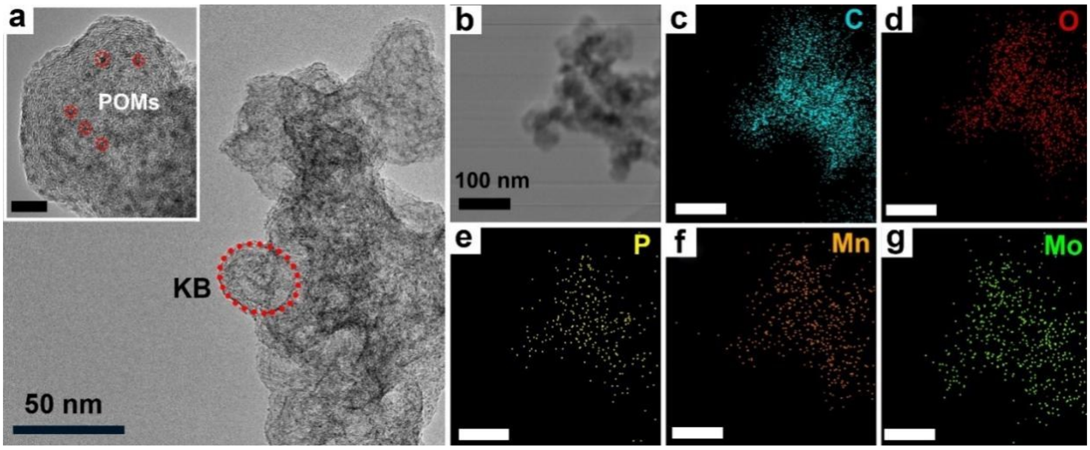

Figure S9 (a) TEM images of **PMo_{12}-MnL** loaded on KB (inset: HR-TEM images of **PMo_{12}-MnL/KB**, scale bar: 5 nm). (b–g) Corresponding elemental mapping of C, O, P, Mn and Mo of **PMo_{12}-MnL/KB**.

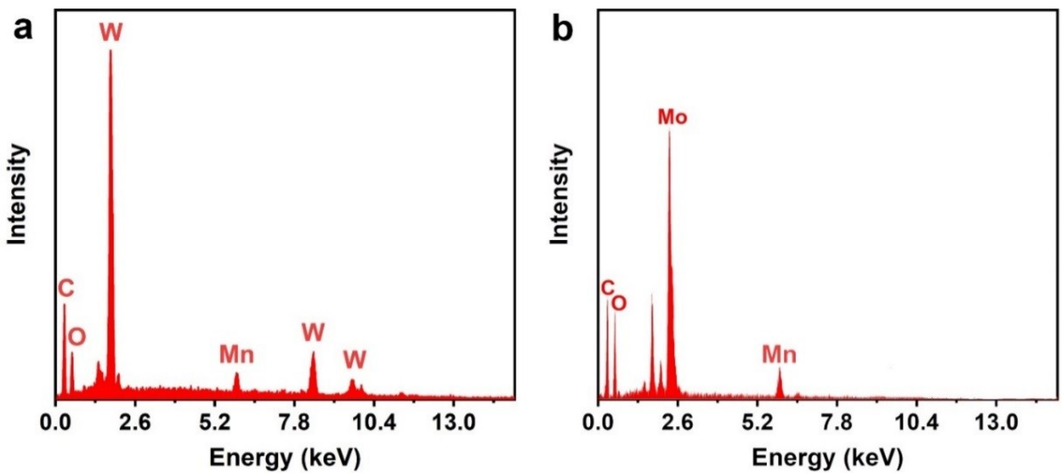

Figure S10 the EDX spectrum of **PW_{12}-MnL/KB** (a) and **PMo_{12}-MnL/KB** (b).

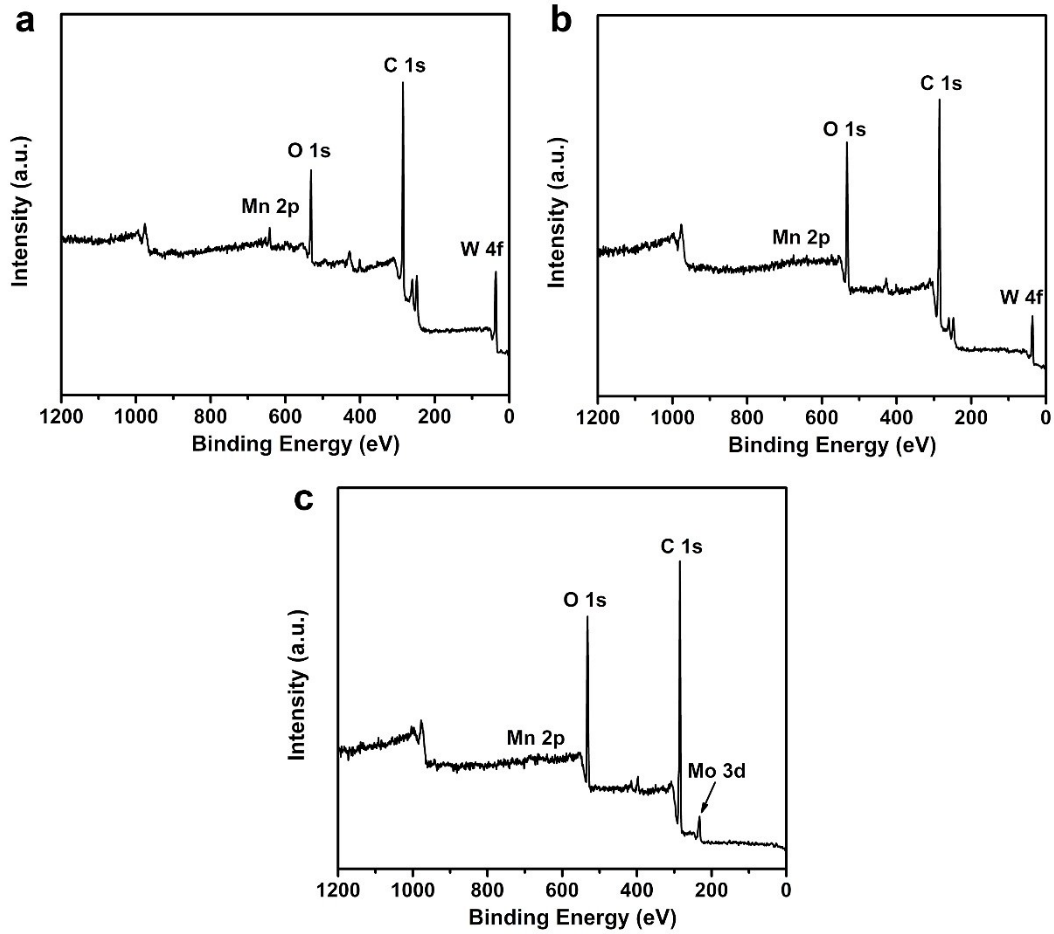

Figure S11 the XPS spectrum of **SiW_{12}-MnL/KB** (a), **PW_{12}-MnL/KB** (b) and **PMo_{12}-MnL/KB** (c).

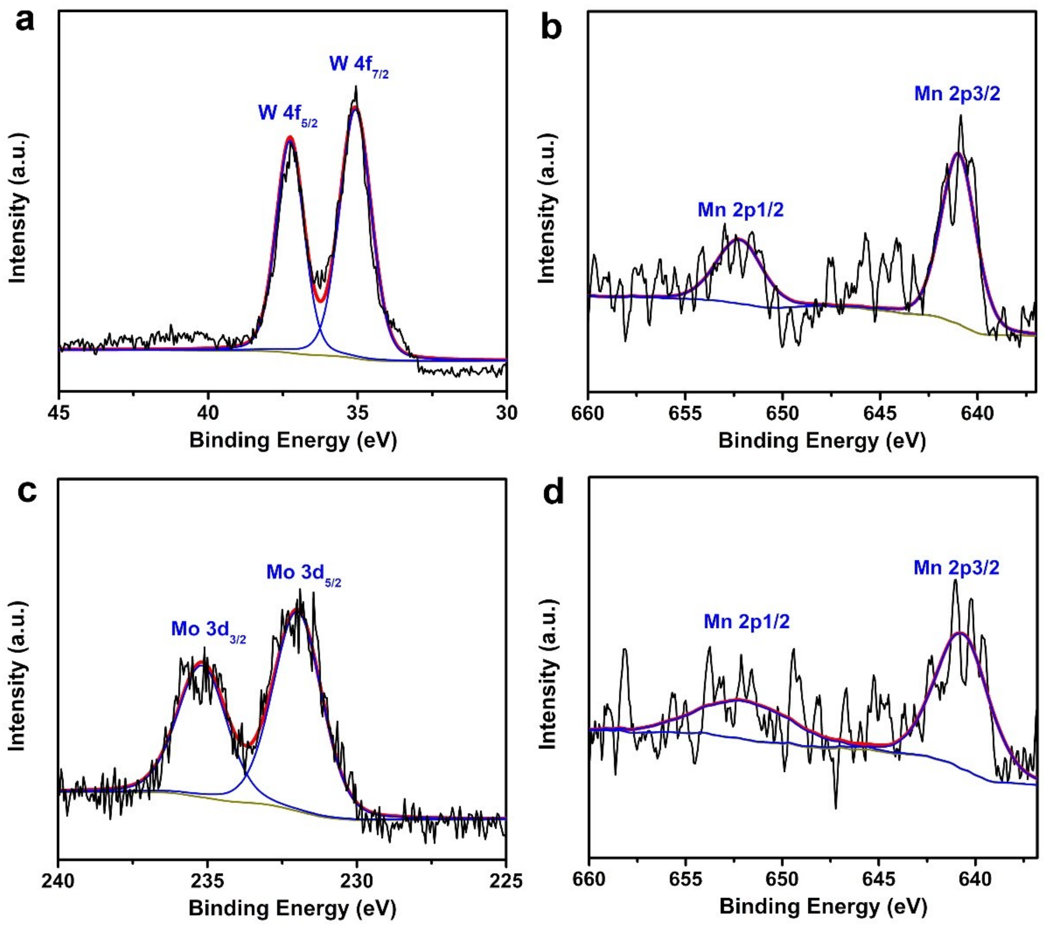

Figure S12 the XPS spectra of **PW_{12}-MnL/KB**: (a) W, (b) Mn; the XPS spectra of **PMo_{12}-MnL/KB**: (c) Mo, (d) Mn.

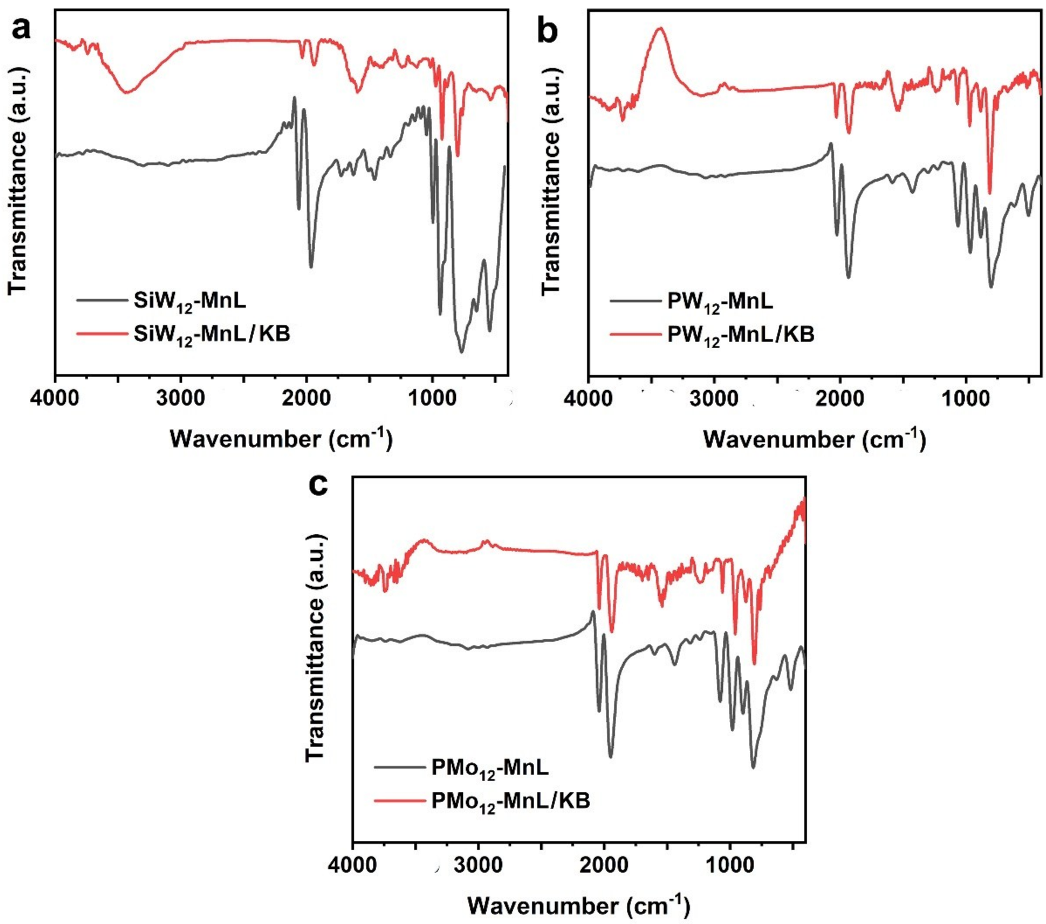

Figure S13 The IR spectrum of **POMs-MnL/KB** and **POMs-MnL/KB**.

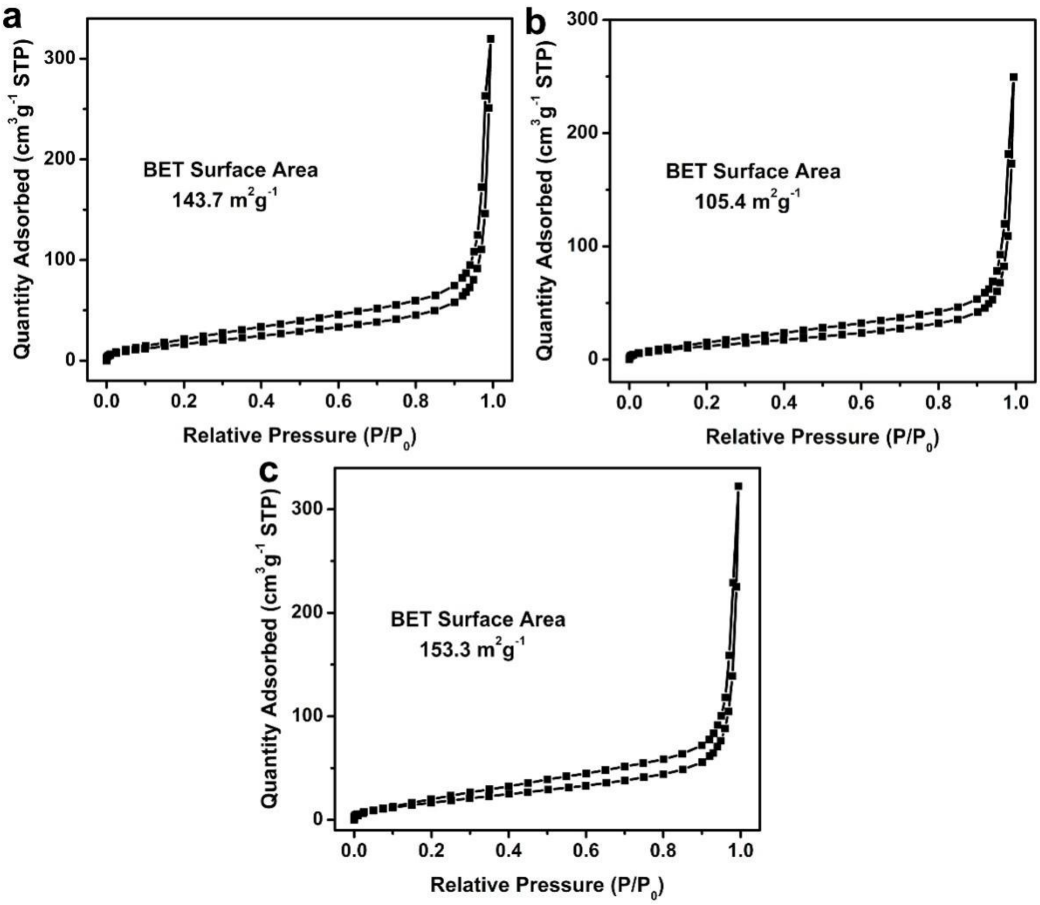

Figure S14 The N_2 sorption isotherms of **POMs-MnL/KB**.

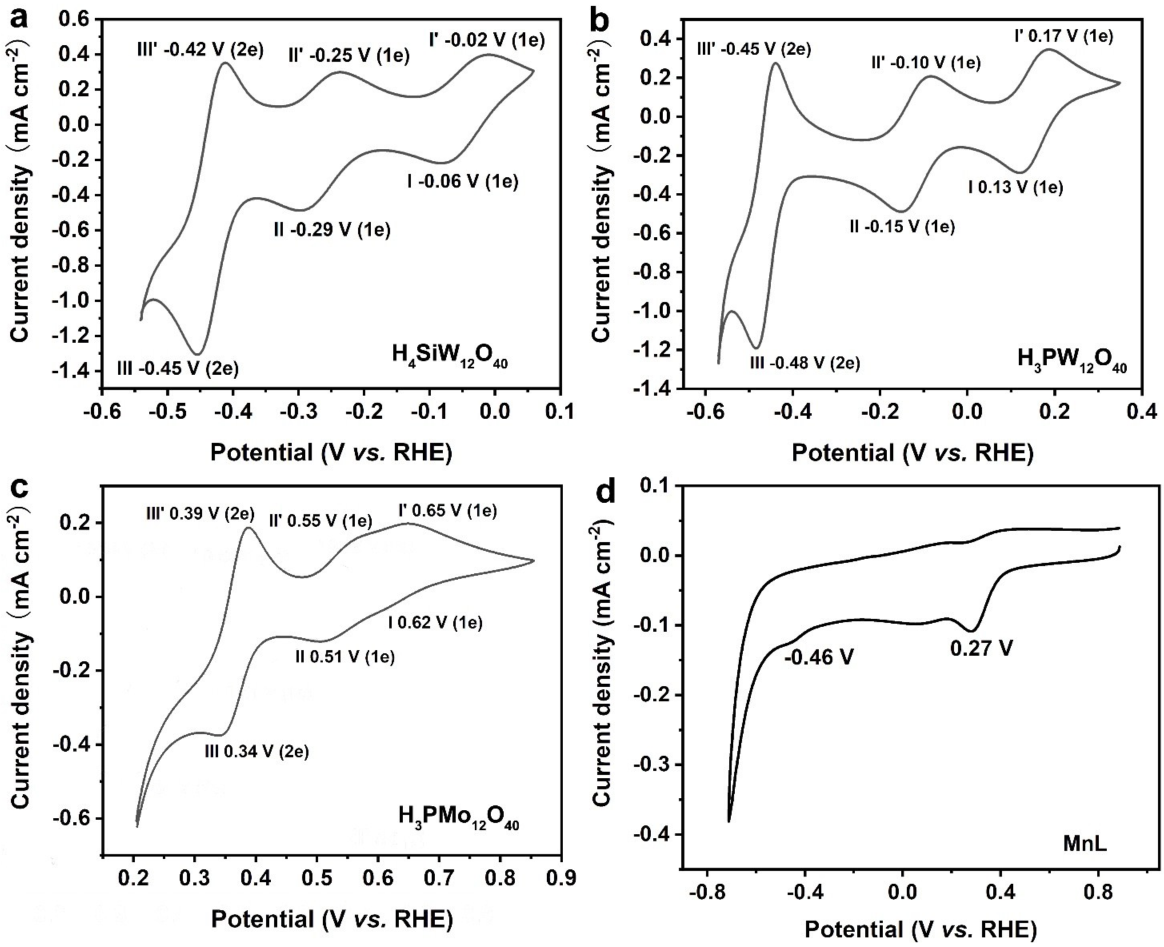

Figure S15 The CV curves of $H_4SiW_{12}O_{40}$(a), $H_3PW_{12}O_{40}$ (b) , $H_3PMo_{12}O_{40}$ (c) in 0.5 mol L^{-1} H_2SO_4 solution (pH 0.3) and MnL in 0.5 mol L^{-1} $KHCO_3$ (pH 8.2) solution at 0.05 V s^{-1} scan rate.

The detailed electron-transfer processes can be expressed as followed [15-18]:

For SiW_{12}

$[SiW_{12}]^{4-}$ + e → $[SiM_{12}]^{5-}$ (E_{redI} = -0.06 V vs. RHE)

$[SiW_{12}]^{5-}$ + e → $[SiM_{12}]^{6-}$ (E_{redII} = -0.29 V vs. RHE)

$[SiM_{12}]^{6-}$ + 2e → $[SiM_{12}]^{8-}$ (E_{redIII} = -0.45 V vs. RHE)

For PW_{12}/PMo_{12}:

$[PM_{12}]^{3-}$ + e → $[PM_{12}]^{4-}$ (E_{redI} = 0.13 V for PW_{12} and E_{redI} = 0.61 V vs. RHE for PMo_{12})

$[PM_{12}]^{4-}$ + e → $[PM_{12}]^{5-}$(E_{redII} = -0.15 V for PW_{12} and E_{redII} = 0.51 V vs. RHE for PMo_{12})

$[PM_{12}]^{5-} + 2e \rightarrow [PM_{12}]^{7-}$ (E_{redIII} = -0.48 V for PW_{12} and E_{redIII} = 0.34 V vs. RHE for PMo_{12})

For MnL:

$[Mn(L)(CO)_3Br]$+e → $[Mn(L^{\bullet -})(CO)_3Br]^-$ (E_{red} = 0.27 V vs. RHE)

$[Mn(L)(CO)_3Br]^-$ +e → $[Mn(L)(CO)_3]^-$ (E_{red} = -0.46 V vs. RHE, the catalytically active species)

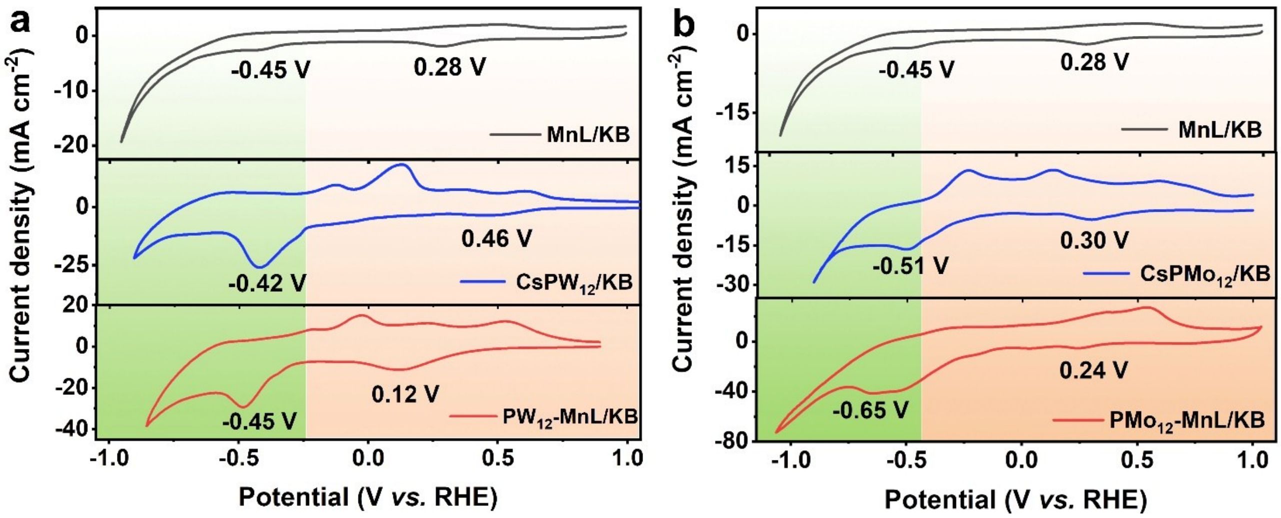

Figure S16 The CVs for MnL/KB, $CsPW_{12}$/KB and PW_{12}-MnL/KB (a) and for MnL/KB, $CsPMo_{12}$/KB and PMo_{12}-MnL/KB (b) in 0.5 mol L^{-1} N_2-saturated $KHCO_3$ at 0.05 V s^{-1} scan rate.

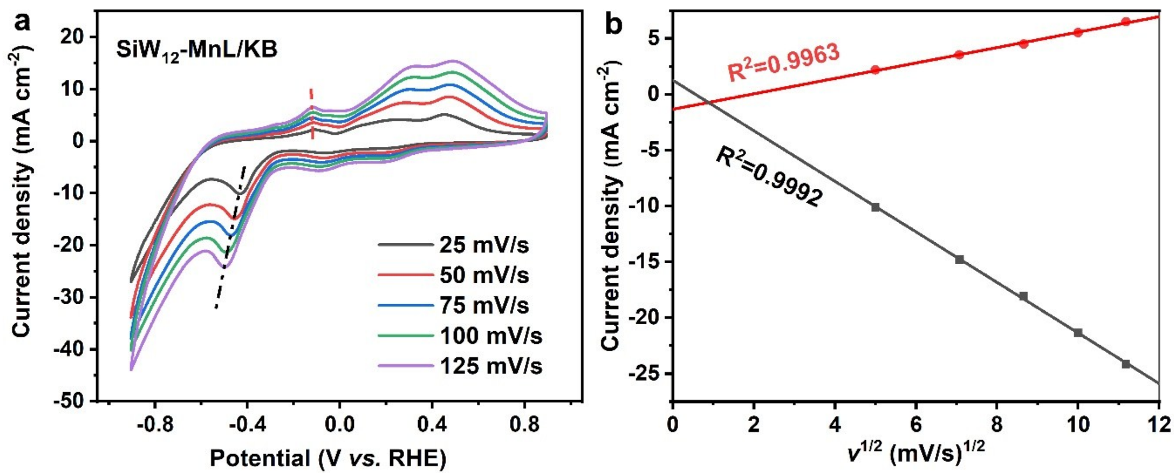

Figure 17 (a) The CVs for SiW_{12}-MnL/KB in 0.5 mol L^{-1} N_2-saturated $KHCO_3$ at different scan rate, (b) graph of peak current *vs*. square root of the scan rate.

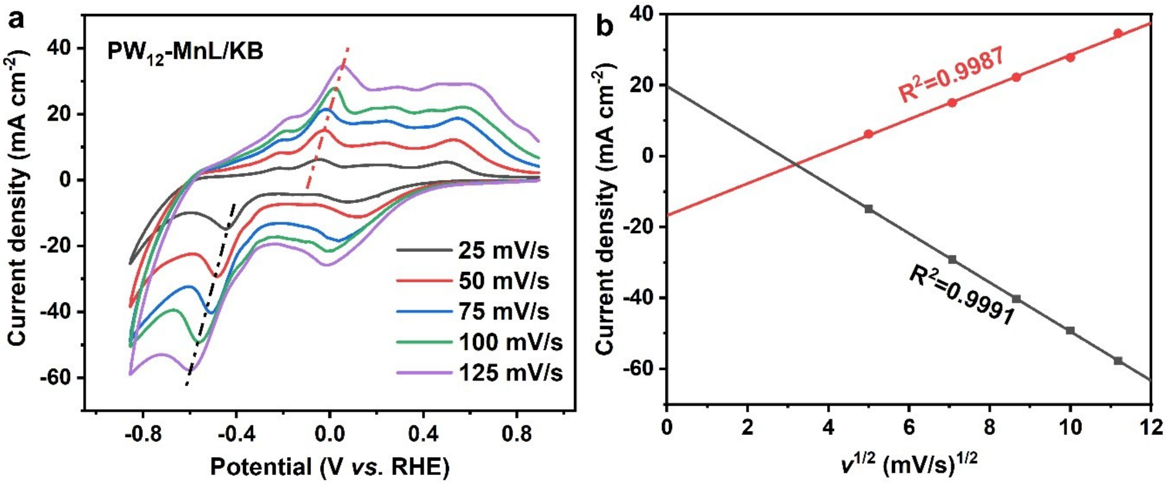

Figure 18 (a) The CVs for PW_{12}-MnL/KB in 0.5 mol L^{-1} N_2-saturated $KHCO_3$ at different scan rate, (b) graph of peak current *vs*. square root of the scan rate.

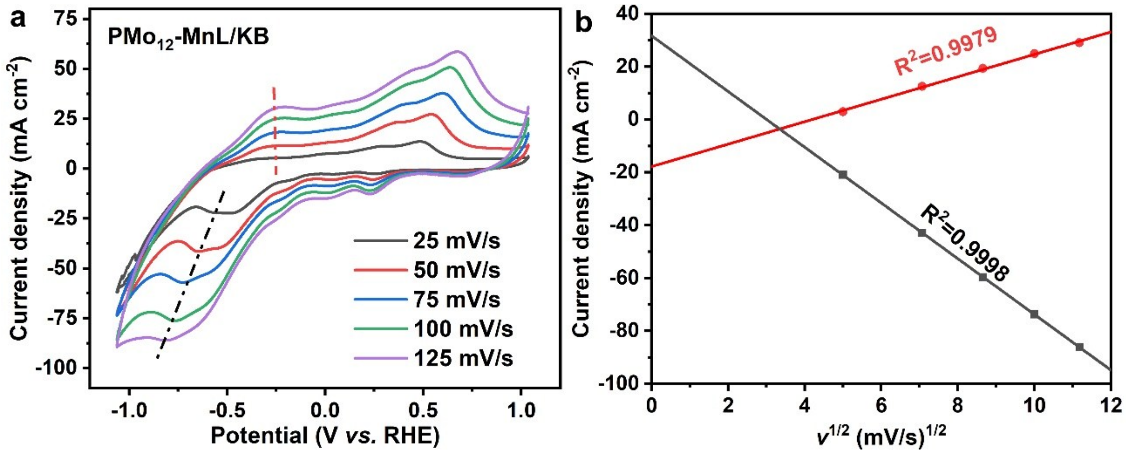

Figure 19 (a) The CVs for PMo_{12}-MnL/KB in 0.5 mol L^{-1} N_2-saturated $KHCO_3$ at different scan rate, (b) graph of peak current *vs*. square root of the scan rate.

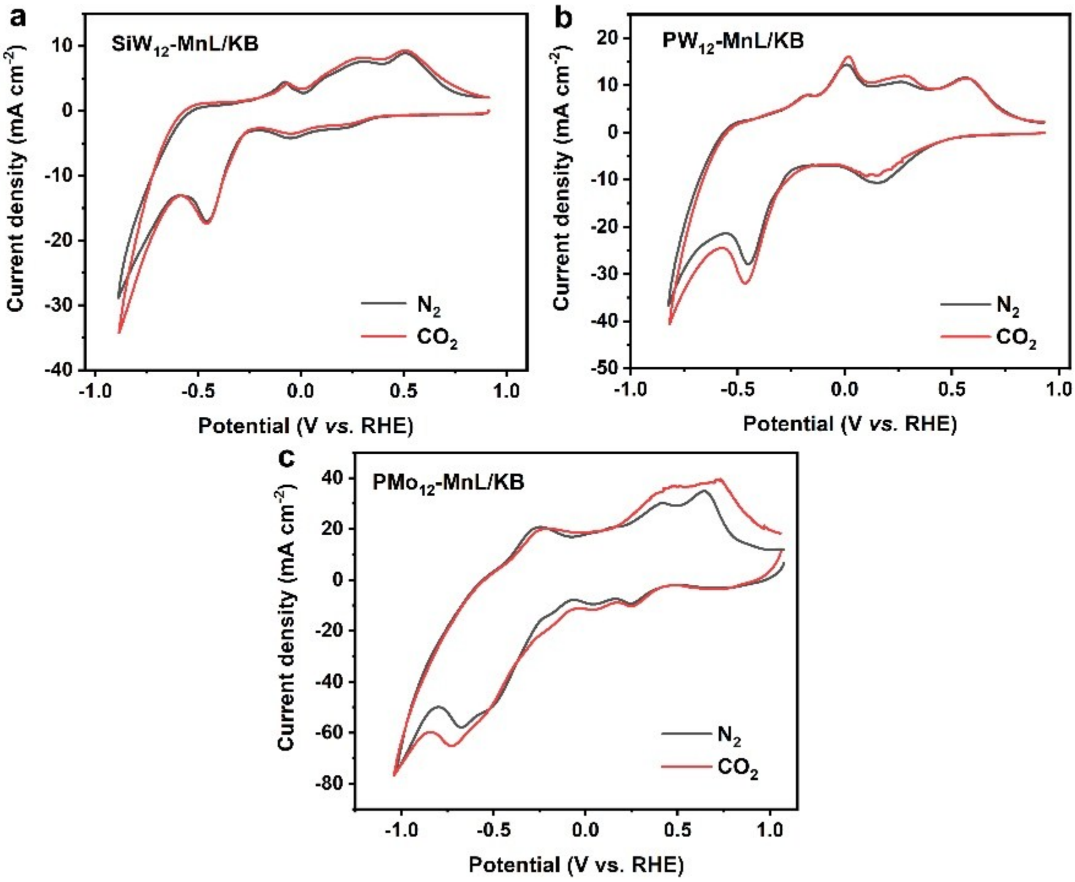

Figure 20 The CV curves of SiW_{12}-MnL/KB (a), PW_{12}-MnL/KB (b) and PMo_{12}-MnL/KB (c) in 0.5 M N_2-(black curve) or CO_2- (red curve) saturated $KHCO_3$ electrolyte.

In Figure S20, the CV curves of POM-MnL/KB in CO_2- and N_2- saturated $KHCO_3$ solution were measured. As shown in Fig. S20, POMs-MnL/KB exhibits consistent electrochemical behavior in N_2- or CO_2-saturated $KHCO_3$ solutions. When the potential is negative then about -0.25 V vs. RHE, the reduction current under the CO_2 saturated condition starts to increase compared to that of in N_2 saturated condition, which means that under this potential range, electrocatalytic CO_2 reduction will occur.

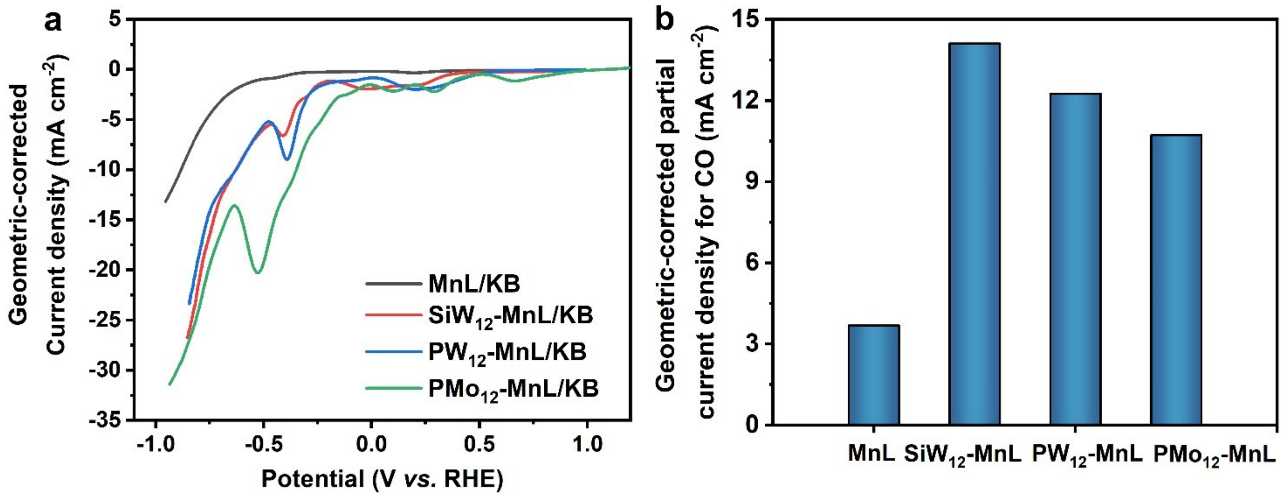

Figure S21 (a) The geometric-corrected current density for MnL/KB and POMs-MnL/KB in 0.5 mol L^{-1} CO_2-saturated $KHCO_3$, (b) The geometric area-corrected current densities for CO of POM-MnL/KB and MnL/KB.

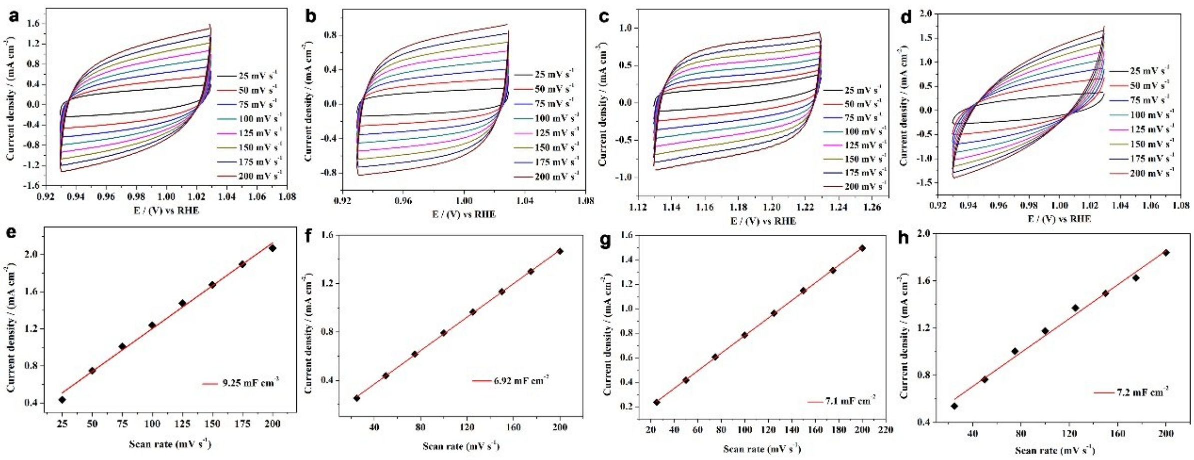

Figure S22 The CV curve of SiW_{12}-MnL/KB (a), PW_{12}-MnL/KB (b), PMo_{12}-MnL/KB (c) and MnL/KB (d) in the potential range without redox current peaks; the linear fitting of Δj vs. scan rates of SiW_{12}-MnL/KB (e), PW_{12}-MnL/KB (f), PMo_{12}-MnL/KB (g) and MnL/KB (h).

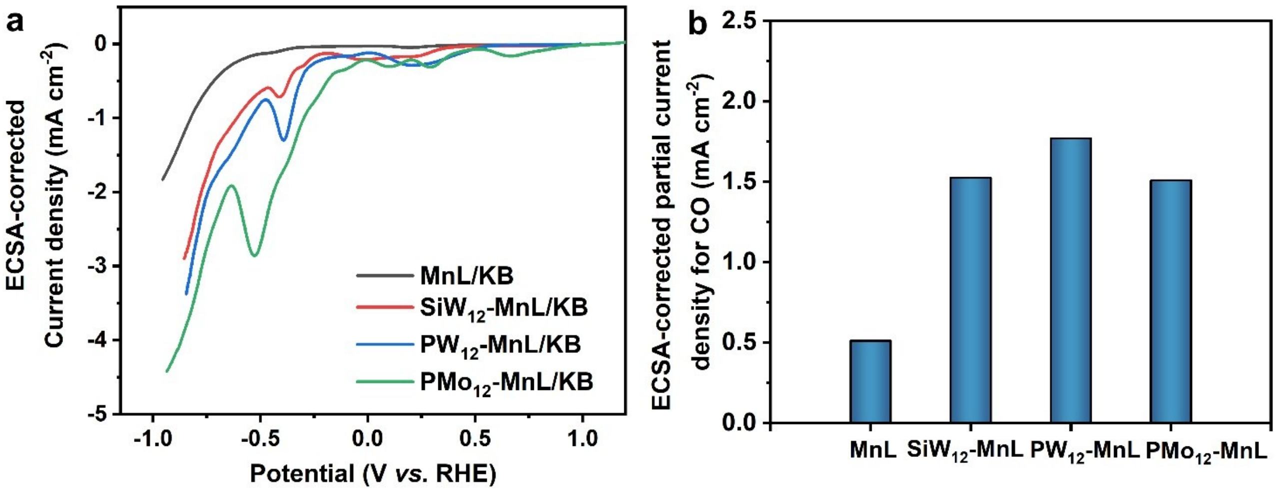

Figure S23 (a) The ECSA-corrected current density for MnL/KB and POMs-MnL/KB in 0.5 mol L^{-1} CO_2-saturated $KHCO_3$, (b) The ECSA-corrected current densities for CO of POM-MnL/KB and MnL/KB.

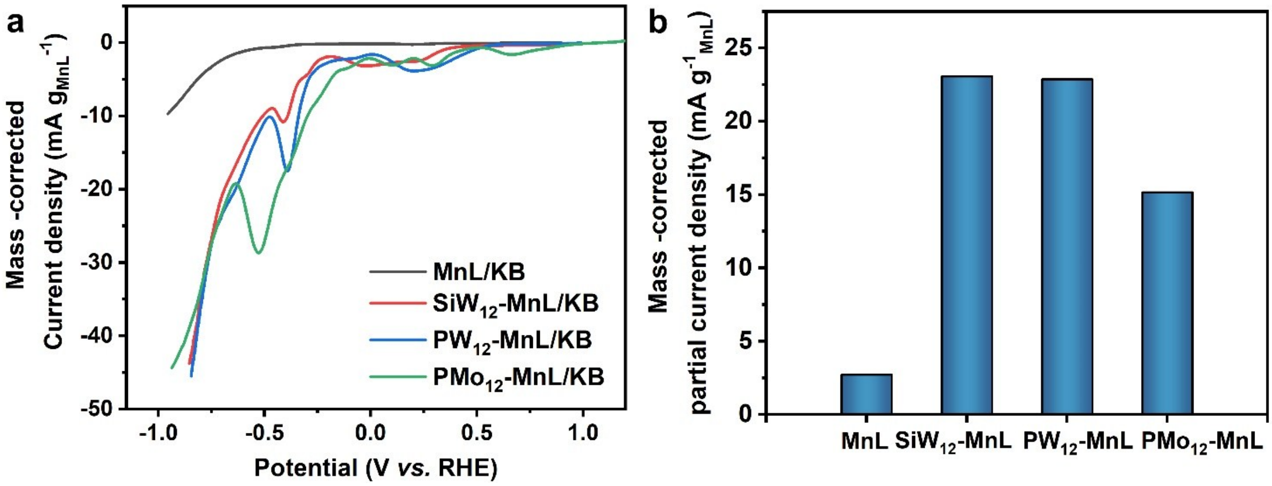

Figure S24 (a) The mass activity (current per catalyst mass)-corrected current density for MnL/KB and POMs-MnL/KB in 0.5 mol L^{-1} CO_2-saturated $KHCO_3$, (b) The mass activity (current per catalyst mass)-corrected current densities for CO of POM-MnL/KB and MnL/KB.

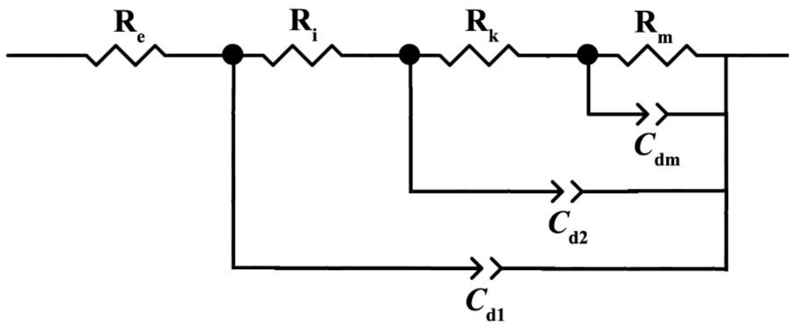

Figure S25 The equivalent circuit model.

The equivalent circuit model includes electrolyte resistance (R_e), electronic resistance (R_i) of the electrode materials and the faradic impedance (Z_f). The The double layer capacitance is distributed between the ohmic and faradaic processes and represented by $C_{d1}$and C_{d2}, respectively. The faradaic impedance can be further divided into a kinetic resistance (R_k) and a mass transfer impedance (Z_m). The mass transfer impedance consists of mass transfer resistance (R_m) and capacitance (C_m).

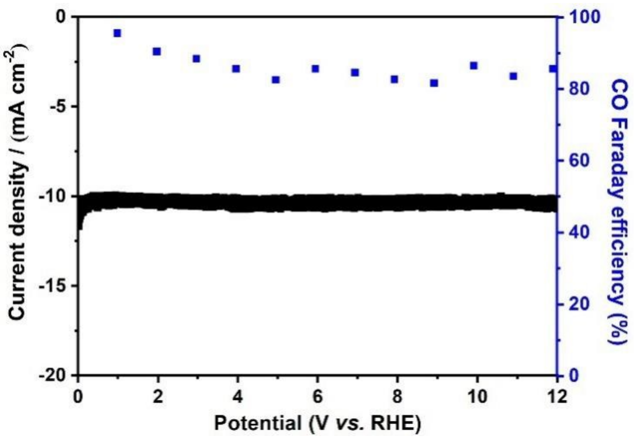

Figure S26 Changes in current density and FE of SiW_{12}-MnL loaded on KB over 12 h at -0.72 V (η = 0.61).

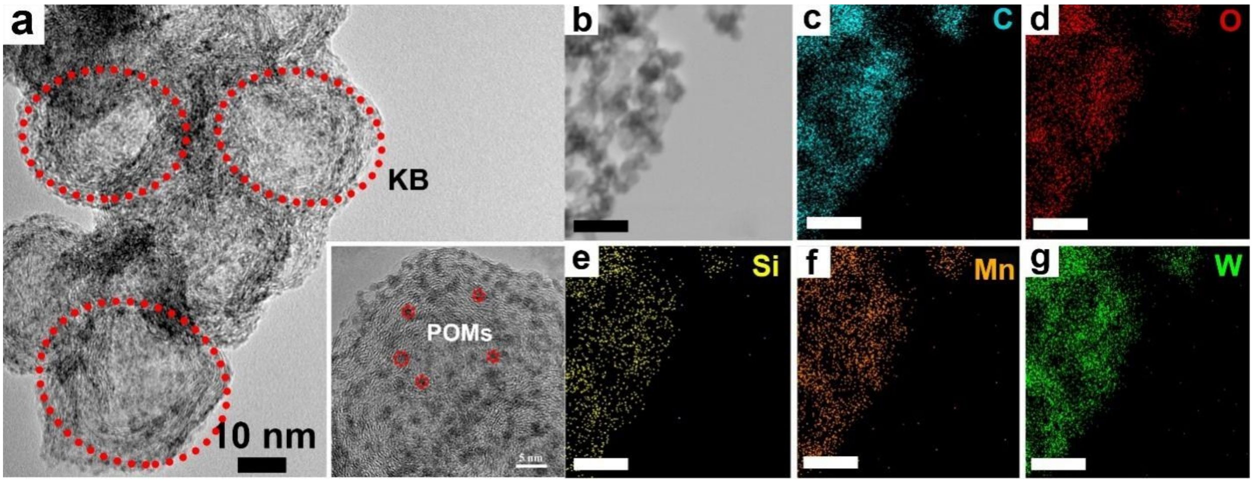

Figure S27 (a) TEM images of SiW_{12}-MnL/KB after the catalytic reactions (inset: HR-TEM images of SiW_{12}-MnL after the catalytic). (b–g) Corresponding elemental mapping of C, O, Si, Mn and W of SiW_{12}-MnL/KB after the catalytic reactions.

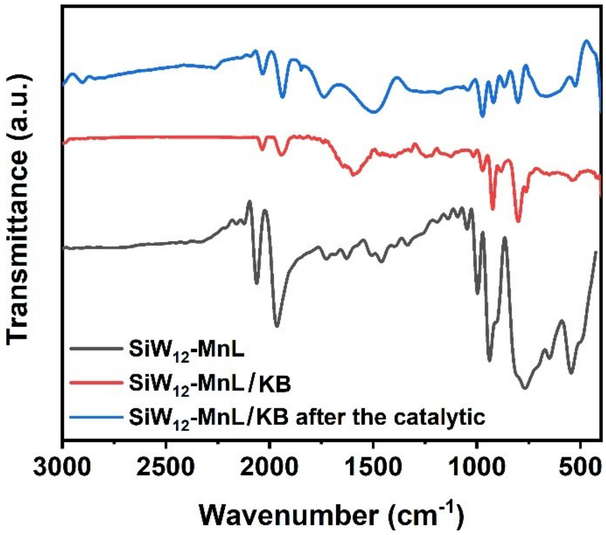

Figure S28 IR spectra of **SiW_{12}-MnL**, **SiW_{12}-MnL**/KB and **SiW_{12}-MnL**/KB after catalytic reactions.

After electrocatalytic CO_2 reduction, the carbonyl characteristic peak at 2250 to 1750 cm^{-1} and the $\{SiW_{12}\}$ characteristic peak at 1250 to 750 cm^{-1} of SiW_{12}-MnL/KB are remained, which indicated that SiW_{12}-MnL is still stable after catalysis. The change of the peaks at 1750 to 1250 cm^{-1} is caused by the removal of the acetonitrile ligand on the manganese carbonyl component after CO_2 reduction.

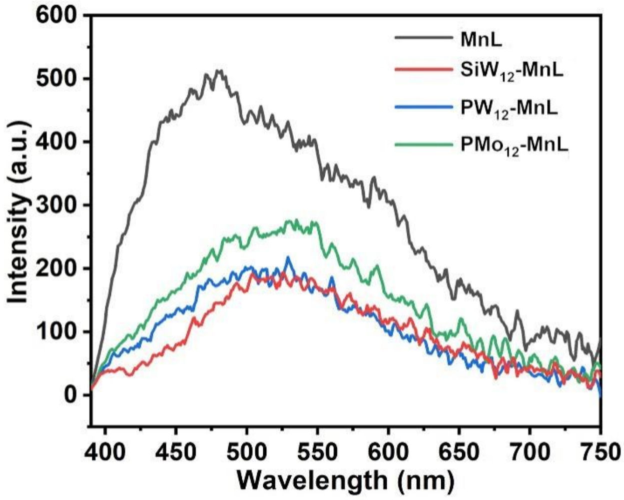

Figure S29 the fluorescence diagram of MnL and POM-MnL (λ_{ex}= 380 nm)

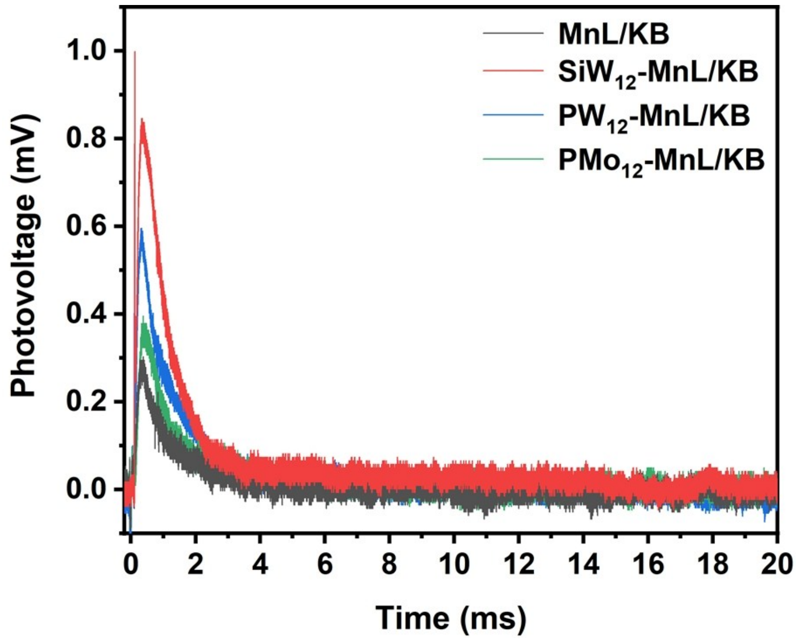

Figure S30 The POM-MnL/KB and MnL/KB in electrode in N_2-saturated $KHCO_3$ aqueous solution.

3. Supplementary Tables

Table S1 Crystal and refinement data for **SiW_{12}-MnL**, **PW_{12}-MnL** and **PMo_{12}-MnL**.

	SiW_{12}-MnL	**PW_{12}-MnL**	**PMo_{12}-MnL**
Formula	$C_{70}H_{61}Mn_4N_{17}O_{52}SiW_{12}$	$C_{49}H_{39}Mn_3N_{11}O_{49}PW_{12}$	$C_{49}H_{39}Mn_3Mo_{12}N_{11}O_{49}P$
Formula weight	4221.14	3967.78	2912.98
Temperature/K	299.15	173.15	273.15
Wavelength/Å	0.71073	0.71073	0.71073
Crystal system	Monoclinic	Triclinic	Triclinic
Space group	*C2/c*	*P-1*	*P-1*
a, b, c/Å	24.8686(19), 23.1581(19), 17.7369(15)	13.0328(5), 15.6142(5), 20.1424(7)	13.0340(6), 15.6737(6), 20.2719(9)
α, β, γ/°	90, 98.907(3), 90	79.8800(10), 89.029(2), 86.775(2)	79.875(2), 88.908(2), 87.011(2)
V/Å^3, Z	10091.7(14), 4	4028.6(2), 2	4071.1(3), 2
D_c/g cm^{-3}, F_{000}	2.778, 7632.0	3.271, 3559.0	2.376, 2792.0
GOF	1.156	1.039	1.036
Reflections collected	55193	60811	74286
R_{int}	0.0791	0.0757	0.0736
θ Range/°	2.325 to 24.999	2.242 to 24.999	2.229 to 25.000
$R_1(I > 2\sigma(I))$ [a]	0.0537	0.0392	0.0442
wR_2 (all data)[a]	0.1407	0.0969	0.0942

[a] $R_1 = \sum||F_0| - |F_C||/\sum|F_0|$; $wR_2 = \sum[w(F_0^2 - F_C^2)^2]/\sum[w(F_0^2)^2]^{1/2}$

Table S2 Selected bond lengths and angles for compound **SiW_{12}-MnL**.

Bond	Length (Å)	Bond	Length (Å)	Bond	Length (Å)
Mn1-N1	2.080(18)	Mn2-C16	1.78(3)	Mn2-N9	2.11(5)
Mn1-N2	2.060(16)	Mn2-C17	1.81(3)	Mn2-N7	1.93(5)
Mn1-N3	1.976(18)	Mn2-C18	1.78(3)	Mn2-N8	2.21(4)
Mn1-C3	1.82(3)	Mn2-N5	2.17(5)		
Mn1-C2	1.79(3)	Mn2-N4	1.90(5)		
Mn1-C1	1.80(3)	Mn2-N6	1.93(3)		
Bond	**Angle (º)**	**Bond**	**Angle (º)**	**Bond**	**Angle (º)**
N2-Mn1-N1	78.8(7)	C16-Mn2-N8	178.0(14)	C18-Mn2-N5	178.7(16)
N3-Mn1-N1	82.7(7)	C17-Mn2-N9	173.4(16)	C18-Mn2-N7	168.5(13)
C3-Mn1-N3	175.6(9)	N4-Mn2-N5	81.2(18)	N7-Mn2-N9	81(2)
C1-Mn1-N2	175.7(10)	N4-Mn2-N6	71.3(17)	N7-Mn2-N8	77.9(12)

Table S3 Selected bond lengths and angles for compound **PW_{12}-MnL**.

Bond	Length (Å)	Bond	Length (Å)	Bond	Length (Å)
Mn1-C1	1.837(14)	Mn2-C26	1.795(14)	Mn3-C33	1.802(15)
Mn1-C3	1.807(15)	Mn2-C27	1.819(13)	Mn3-C32	1.809(15)
Mn1-C2	1.825(14)	Mn2-C28	1.831(14)	Mn3-C31	1.766(16)
Mn1-N7	2.013(10)	Mn2-N9	2.016(11)	Mn3-N8	2.004(13)
Mn1-N1	2.055(10)	Mn2-N4	2.033(10)	Mn3-N6	2.047(10)
Mn1-N2	2.033(10)	Mn2-N3	2.053(10)	Mn3-N5	2.022(10)
Bond	**Angle (º)**	**Bond**	**Angle (º)**	**Bond**	**Angle (º)**
N7-Mn1-N2	82.3(4)	N9-Mn2-N3	85.1(4)	N8-Mn3-N6	84.2(4)
N2-Mn1-N1	78.9(4)	N4-Mn2-N3	78.7(4)	N5-Mn3-N6	79.2(4)
C1-Mn1-N2	175.0(5)	C26-Mn2-N4	175.7(5)	C33-Mn3-N8	175.4(6)
C2-Mn1-N7	176.5(5)	C28-Mn2-N9	178.0(5)	C31-Mn3-N5	175.5(6)

Table S4 Selected bond lengths and angles for compound **PMo_{12}-MnL**.

Bond	Length (Å)	Bond	Length (Å)	Bond	Length (Å)
Mn2-C18	1.814(8)	Mn3-N9	2.011(6)	Mn1-N2	2.034(5)
Mn2-N4	2.045(5)	Mn3-N5	2.051(5)	Mn1-N1	2.039(5)
Mn2-N3	2.055(5)	Mn3-N6	2.034(6)	Mn1-C1	1.799(8)
Mn2-N8	2.030(6)	Mn3-C31	1.793(9)	Mn1-N7	2.011(7)
Mn2-C17	1.797(9)	Mn3-C33	1.812(9)	Mn1-C3	1.800(9)
Mn2-C16	1.817(8)	Mn3-C32	1.803(8)	Mn1-C2	1.798(10)
Bond	Angle (º)	Bond	Angle (º)	Bond	Angle (º)
C18-Mn2-N8	178.5(3)	N9-Mn3-N6	83.5(2)	N2-Mn1-N1	79.2(2)
N4-Mn2-N3	78.9(2)	N6-Mn3-N5	78.9(2)	C1-Mn1-N7	174.4(3)
N8-Mn2-N3	86.1(2)	C33-Mn3-N9	177.2(3)	N7-Mn1-N1	84.1(2)
C17-Mn2-N4	175.7(3)	C32-Mn3-N6	175.6(3)	C3-Mn1-N1	174.8(4)

Table S5 Hydrogen bonds for **SiW_{12}-MnL**.

D–H···A	d(D–H) (Å)	d(H···A) (Å)	d(D···A) (Å)	∠(DHA) (º)
C9-H9...O3#1	0.93	2.50	3.21(3)	133.7
C12-H12...O5#1	0.93	2.47	3.32(3)	152.3
N6-H6B...N4	0.89	1.69	2.24(5)	116.3
C32-H32A...O26#2	0.96	2.37	3.27(7)	154.8
C20-H20A...O4	0.96	2.52	3.40(6)	153.0
C20-H20B...O10#3	0.96	2.44	3.18(6)	133.7
C24-H24...O2	0.93	2.42	3.10(5)	130.5
C22-H22...O6#4	0.93	2.35	3.09(5)	136.7
C22-H22...O7#4	0.93	2.63	3.48(6)	152.6

Symmetry transformations used to generate equivalent atoms: #1 +X,-Y,-1/2+Z; #2 -X,+Y,3/2-Z; #3 1/2-X,1/2-Y,1-Z; #4 +X,-Y,1/2+Z

Table S6 Hydrogen bonds for **PW_{12}-MnL**.

D–H···A	d(D–H) (Å)	d(H···A) (Å)	d(D···A) (Å)	∠(DHA) (º)
C30-H30A...O7#1	0.98	2.58	3.136(16)	115.7
C25-H25...O27#2	0.95	2.53	3.236(14)	131.5
C43-H43...O2	0.95	2.47	3.232(15)	136.9
C40-H40...O28#3	0.95	2.42	3.047(16)	122.9
C40-H40...O17#4	0.95	2.68	3.573(15)	157.0
C15-H15A...O34	0.98	2.59	3.256(16)	125.6
C15-H15B...O13	0.98	2.62	3.522(17)	153.5
C13-H13...O3#5	0.95	2.51	3.337(17)	144.9
C12-H12...O33#5	0.95	2.54	3.283(15)	134.8
C22-H22...O3#1	0.95	2.65	3.334(16)	129.7
C45-H45A...O9#6	0.98	2.63	3.302(19)	126.0
C48-H48B...O23#4	0.98	2.50	3.464(19)	166.3
C46-H46B...O46#5	0.98	2.54	3.48(2)	160.6
C46-H46C...O31	0.98	2.26	3.11(2)	143.9

Symmetry transformations used to generate equivalent atoms: #1 -1+X,+Y,+Z; 2# -1+X,-1+Y,+Z; 3# +X,-1+Y,+Z; 4# 2-X,1-Y,1-Z; 5# 1-X,1-Y,2-Z; 6# 1-X,1-Y,1-Z

Table S7 Hydrogen bonds for **PMo_{12}-MnL**.

D–H···A	d(D–H) (Å)	d(H···A) (Å)	d(D···A) (Å)	∠(DHA) (º)
C7-H7...O3#1	0.93	2.45	3.131(8)	130.4
C4-H4...O27	0.93	2.45	3.189(8)	136.2
C22-H22...O37#2	0.93	2.63	3.336(9)	132.9
C42-H42...O6#3	0.93	2.53	3.276(8)	136.9
C19-H19...O17#4	0.93	2.54	3.229(7)	131.2
C45-H45B...N11#2	0.96	2.62	3.442(15)	143.3
C45-H45C...O26#5	0.96	2.64	3.520(9)	152.4
C45-H45C...O11#5	0.96	2.64	3.458(9)	142.7
C43-H43...O37#3	0.93	2.63	3.447(9)	146.7
C47-H47A...O45#6	0.96	2.55	3.507(15)	175.1
C47-H47C...O15	0.96	2.50	3.088(14)	119.7

Symmetry transformations used to generate equivalent atoms: #1 +X,1+Y,+Z; #2 1-X,1-Y,1-Z; #3 1-X,1-Y,-Z; #4 1-X,-Y,1-Z; #5 -1+X,+Y,+Z; #6 +X,+Y,-1+Z

Table S8 The bond-valence sum (BVS) calculations of W and Mn for **SiW_{12}-MnL/KB**.[a]

Atom	Oxidation states	Atom	Oxidation states
W1	6.22	W4	6.20
W2	6.35	W5	6.17
W3	6.27	W6	6.29

[a] The bond-valence sum (BVS) calculation method is according reference [19].

Table S9 The bond-valence sum (BVS) calculations of W and Mn for **PW_{12}-MnL/KB** and **PMo_{12}-MnL/KB**.[a]

PW_{12}-MnL/KB			
Atom	Oxidation states	Atom	Oxidation states
W1	6.21	W7	6.22
W2	6.14	W8	6.32
W3	6.27	W9	6.24
W4	6.23	W10	6.22
W5	6.26	W11	6.09
W6	6.17	W12	6.23
PMo_{12}-MnL/KB			
Atom	Oxidation states	Atom	Oxidation states
Mo1	6.14	Mo7	6.08
Mo2	6.09	Mo8	6.10
Mo3	6.09	Mo9	6.11
Mo4	6.09	Mo10	6.08
Mo5	6.04	Mo11	6.07
Mo6	6.13	Mo12	6.05

[a] The bond-valence sum (BVS) calculation method is according reference [19].

Table S10 Equivalent circuit parameters of POMs-MnL/KB and MnL/KB

Electrocatalysts	R_e / ohm cm^2	R_i / ohm cm^2	R_k / ohm cm^2	R_m / ohm cm^2
MnL/KB	0.4422	2.931	3.407	40.86
SiW_{12}-MnL/KB	0.4847	2.347	0.539	16.18
PW_{12}-MnL/KB	0.407	2.363	6.745	29.67
PMo_{12}-MnL/KB	0.4429	1.821	0.4947	5.645

4. References

[1] O. V. Dolomanov, L. J. Bourhis, R. J. Gildea, J. A. K. Howard, H. Puschmann, *J. Appl. Cryst.* **2009**, *42*, 339.

[2] G. Sheldrick, *Acta Cryst. A* **2008**, *64*, 112.

[3] G. Sheldrick, *Acta Cryst. C* **2015**, *71*, 3.

[4] A. Spek, *Acta Cryst. C* **2015**, *71*, 9.

[5] N. Han, Y. Wang, L. Ma, J. Wen, J. Li, H. Zheng, K. Nie, X. Wang, F. Zhao, Y. Li, J. Fan, J. Zhong, T. Wu, D. J. Miller, J. Lu, S.-T. Lee, Y. Li, *Chem.* **2017**, *3*, 652.

[6] M. Frisch, G. Trucks, H. Schlegel, G. Scuseria, M. Robb, J. Cheeseman, G. Scalmani, V. Barone, B. Mennucci, G. Petersson, *Gaussian09W Revision D. 01, Gaussian Inc. Wallingford CT. 2009*.

[7] A. D. Becke, *J. Chem. Phys.* **1993**, *98*, 5648.

[8] C. Lee, W. Yang, R. G. Parr, *Phys. Rev. B* **1988**, *37*, 785.

[9] P. J. Hay, W. R. Wadt, *J. Chem. Phys.* **1985**, *82*, 270.

[10] M. M. Francl, W. J. Pietro, W. J. Hehre, J. S. Binkley, M. S. Gordon, D. J. DeFrees, J. A. Pople, *J. Chem. Phys.* **1982**, *77*, 3654.

[11] P. C. Hariharan, J. A. Pople, *Theor. Chim. Acta* **1973**, *28*, 213-222.

[12] G. A. Petersson, M. A. Al-Laham, *J. Chem. Phys.* **1991**, *94*, 6081.

[13] S. Grimme, S. Ehrlich, L. Goerigk, *J. Comput. Chem.* **2011**, *32*, 1456.

[14] J. Tomasi, B. Mennucci, R. Cammi, *Chem. Rev.* **2005**, *105*, 2999.

[15] J. Friedl, M. V. Holland-Cunz, F. Cording, F. L. Pfanschilling, C. Wills, W. McFarlane, B. Schricker, R. Fleck, H. Wolfschmidt and U. Stimming, *Energ. Environ. Sci.*, 2018, **11**, 3010.

[16] J. Xie, P. Yang, Y. Wang, T. Qi, Y. Lei and C. M. Li, *J. Power Sources*, 2018, **401**, 213.

[17] M. Bourrez, F. Molton, S. Chardon-Noblat and A. Deronzier, *Angew. Chem. Int. Ed. Engl.*, 2011, 50, 9903

[18] J. J. Walsh, C. L. Smith, G. Neri, G. F. Whitehead, C. M. Robertson and A. J. Cowan, *Farad. Disc.*, 2015, **183**, 147.

[19] I. B. Brown, D. Altermatt, *Acta Cryst. Sect B* **1976**, *32*, 1957.